CNRS
Centre National de la Recherche Scientifique

INFN
Istituto Nazionale di Fisica Nucleare

Effects of CITF misalignments on the longitudinal error signals during the CARM offset phase of AdV+.

VIR-0446A-20

Michele Valentini[1, 2*], Julia Casanueva[3], Maddalena Mantovani[3], and Antonio Perreca[1, 2*]

[1] *University of Trento*
[2] *INFN TIFPA*
[3] *European Gravitational Observatory*

Date: September 5, 2022

[*] *corresponding author:* michele.valentini@unit.it

VIRGO* A joint CNRS-INFN Project
Via E. Amaldi, I-56021 S. Stefano a Macerata - Cascina (Pisa)
Secretariat: Telephone (39) 050 752 521 * FAX (39) 050 752 550 * Email: ego@ego-gw.it

Contents

In the previous Power-Recycled Michelson Interferometer (PRMI) configuration used until O3, the Angular Sensing and Control (ASC) loops were engaged in full-bandwidth mode only at the end of the locking sequence. A study of the error signals for that configuration was previously made in [1], with a focus on the effects of misalignment of the Power Recycling (PR) mirror, crucial for the variable finesse technique.

In the new Dual-Recycled Michelson Interferometer (DRMI) configuration, however, the lock of the Central InTerFerometer (CITF) Degree Of Freedoms (DOFs) is radically different from before. The structure of the new lock acquisition procedure (explained in [2]) raised concerns regarding the feasibility of maintaining the CITF lock for the full duration of the Common ARM length (CARM) offset reduction procedure, which lasts several minutes. During this period, a recycling cavity's alignment drift affecting the longitudinal error signals could ultimately spoil the stability of the lock.

Therefore, we simulated the influence of misalignments of the arm input mirrors, PR, North Input (NI) mirror and Signal Recycling (SR) mirrors on the "3f" CITF longitudinal error signals. Particular focus was given to finding a maximum allowable misalignment for each mirror, above which the stability of the lock cannot be guaranteed. This threshold value has then been used to choose the automatic alignment strategy to use during the CARM offset reduction phase.

1 Simulation details and limits

The simulations have been performed using the modal simulation software Finesse 2 [3].

We used a variation of the simulation setup described in [4].The limits and the observations discussed in that document regarding the capability of that configuration to represent the real interferometer are still applicable to these simulations. The main difference in the setup used in this study is the addition of a 1.5 kHz CARM offset. Since during these steps, the arm cavities are off-resonance and controlled by the Auxiliary Laser System (ALS), the influence of small CARM and Differential ARM length (DARM) displacements on the InfraRed (IR) beam is minimal, and the simulations focused on studying the CITF DOFs. Additionally, the study of misaligned components added the necessity of simulating a larger number of Hermite-Gauss modes to correctly represent the laser field in the interferometer.

To optimize the simulation process, the procedure was divided into the following steps:

- Base simulation of misaligned interferometer and convergence check;
- simulation of the longitudinal DOFs sweeps;
- optimization and study of the error signals.

These steps will be explained in detail in sections 1.2-1.4.

1.1 Optimally matched interferometer

Consistently to the studies reported in [4], the simulated interferometer configuration is optimally mode-matched. This is not completely true in the real interferometer during the lock-acquisition, in which the interferometer optics are subject to aberrations called "cold defects" [5].

The choice of simulating an optimally mode-matched interferometer was given for the following reasons:

- Impossibility of having a representative estimate of the non-idealities affecting the CITF error signals before the installation and commissioning of the upgrades, currently ongoing.
- The overall impact of misalignments is maximum in the ideally matched configuration. A likely explanation is that in the ideal configuration, the studied misalignments are the only source of Higher Order Modes (HOMs) contributing to the error signals' degradation. An additional presence of losses toward HOMs given by mismatch and other cold defects mitigates the impact of the misalignment by preemptively lowering the finesse of the cavity for the gaussian components. Therefore, the simulated setup corresponds to the "worst case scenario" regarding the impact of misalignments, making it an ideal choice for this study.

1.2 Base simulation of misaligned interferometer and convergence check

To accurately study the behaviour of the interferometer when subject to misalignments, the correct working points of the Longitudinal Sensing and Control (LSC) DOFs need to be found for each angle of each misaligned mirror. This is accomplished by minimizing the '3f' error signals using the built-in 'lock' command of Finesse. This procedure simulates the action of the CITF LSC loops, which are indeed engaged during the simulated scenario. The found working points are then saved and used for further simulations.

During this step, the convergence of the simulations is also tested. This means estimating whether the amount of Transverse ElectroMagnetic (TEM) HOMs used in the simulation is sufficient to give realistic results. The convergence has been checked by finding the CITF working points with an increasingly higher number of HOMs and then comparing the results. The number of used HOMs is determined by Finesse's 'maxtem' value, which indicates the maximum order of the simulated modes. The results are reported in the top plots of figures 1, 2, and 3 for the misalignment of the PR, NI and SR mirrors, respectively. One can notice that in most cases, the larger the misalignment becomes, the more significant the impact of adding additional HOMs.

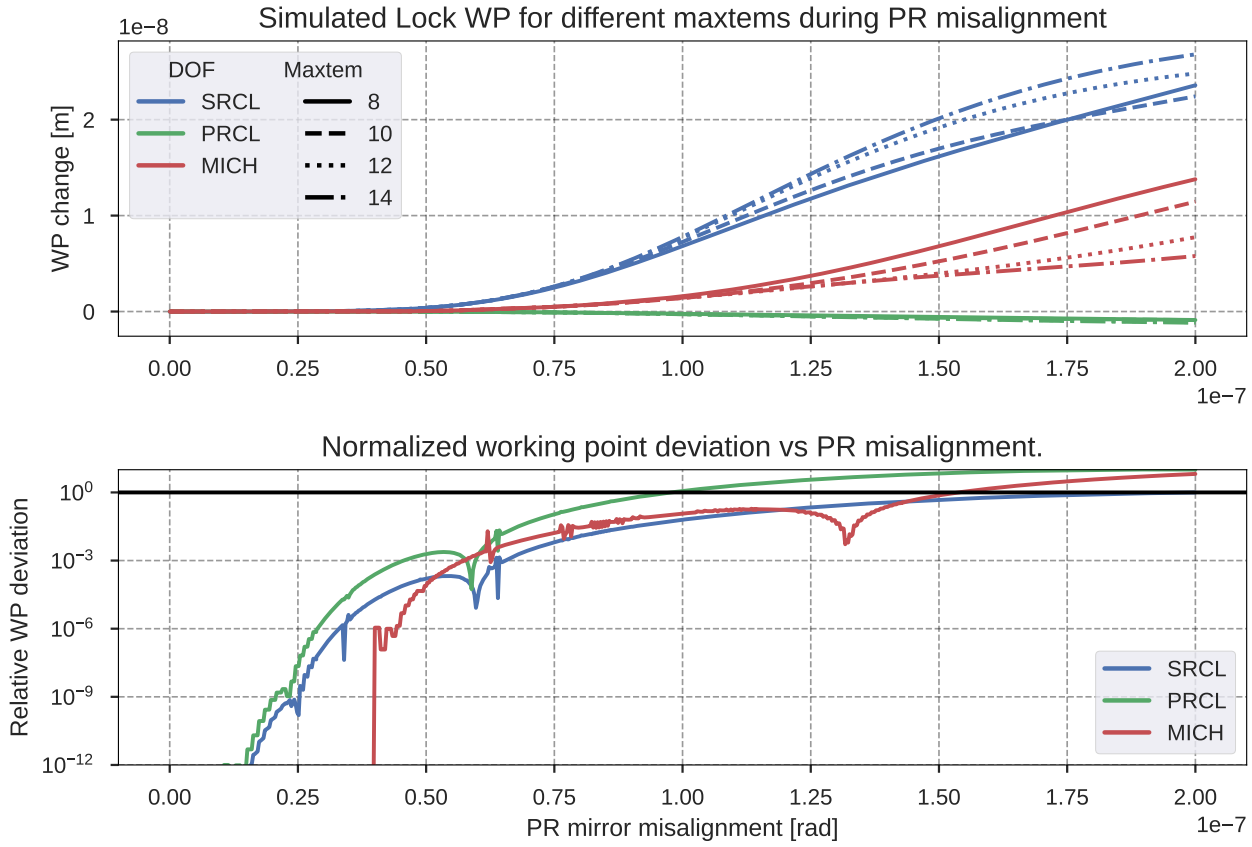

Figure 1: Top: CITF DOFs' simulated Working Points (WPs) during the misalignment of the PR mirror for different 'maxtem' values. The DOFs are 'locked' using the '3f' signals. The 'maxtem' parameter indicates how many Hermite-Gauss HOMs were used in the simulation.
Bottom: Normalized WP differences for misalignments of the PR mirror. The lines indicate the difference in the WPs simulated with 'maxtem' 14 and 'maxtem' 12, normalized by the respective DOF accuracy requirements. Discontinuities in the line are caused by the finite tolerance of the lock algorithm.

An interesting figure of merit to evaluate the convergence is the relative WP variation between a simulation including up to a certain 'maxtem' value and the subsequent one, e.g., the difference between the WP estimated with 'maxtem' 12 and with 'maxtem' 14. This variation is compared with the accuracy requirements values

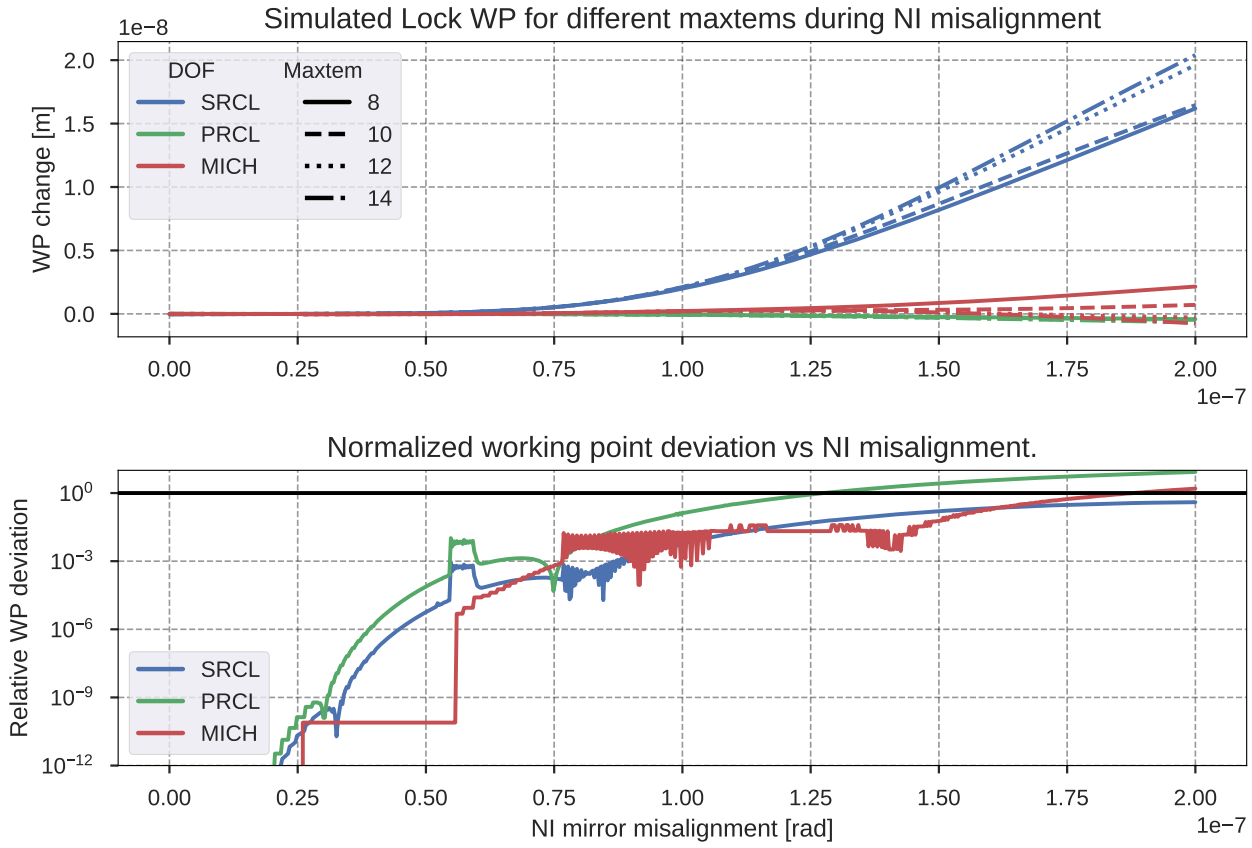

Figure 2: CITF DOFs' simulated WPs during the misalignment of the NI mirror for different 'maxtem' values. The DOFs are 'locked' using the '3f' signals. The 'maxtem' parameter indicates how many Hermite-Gauss HOMs were used in the simulation.
Bottom: Normalized WP differences for misalignments of the NI mirror. The lines indicate the difference in the WPs simulated with 'maxtem' 14 and 'maxtem' 12, normalized by the respective DOF accuracy requirements. Discontinuities in the line are caused by the finite tolerance of the lock algorithm.

discussed in [6]. While these accuracy values were defined for the interferometer in the steady-state condition and can be more relaxed during the CITF phase of the lock acquisition, they are still a good reference value to compare displacements of different DOFs. The results, shown in the bottom plots of figures 1, 2, and 3 (respectively for PR, NI and SR misalignments), show that using maxtem 14, the PR and NI misalignment simulations converge up to $\simeq 1.5 \cdot 10^{-7} rad$ and $\simeq 1.8 \cdot 10^{-7} rad$ respectively. For the misalignment of SR, the simulations converged in all the simulated ranges, up to $\simeq 3 \cdot 10^{-6} rad$. The results of the simulations (in section 2) show that these ranges are sufficient to study the necessity of a high-bandwidth (and gain) automatic alignment control.

Additionally, the optical gain of the error signals and their optimal demodulation phases have also been simulated for multiple maxtems. The results showed, between maxtem 12 and maxtem 14 and up to the angles mentioned above, differences lower than 1% for optical gains and lower than 5° for the optimal demodulation phases, thus not giving additional restrictions in the simulations.

Simulating misalignments and paraxial approximation: A further limitation to the maximum misalignment angle that can be simulated is given by the validity of Finesse's paraxial approximation. In particular, the misalignment of the cavity should not be above the beam's diffraction angle Θ. The diffraction angle is defined

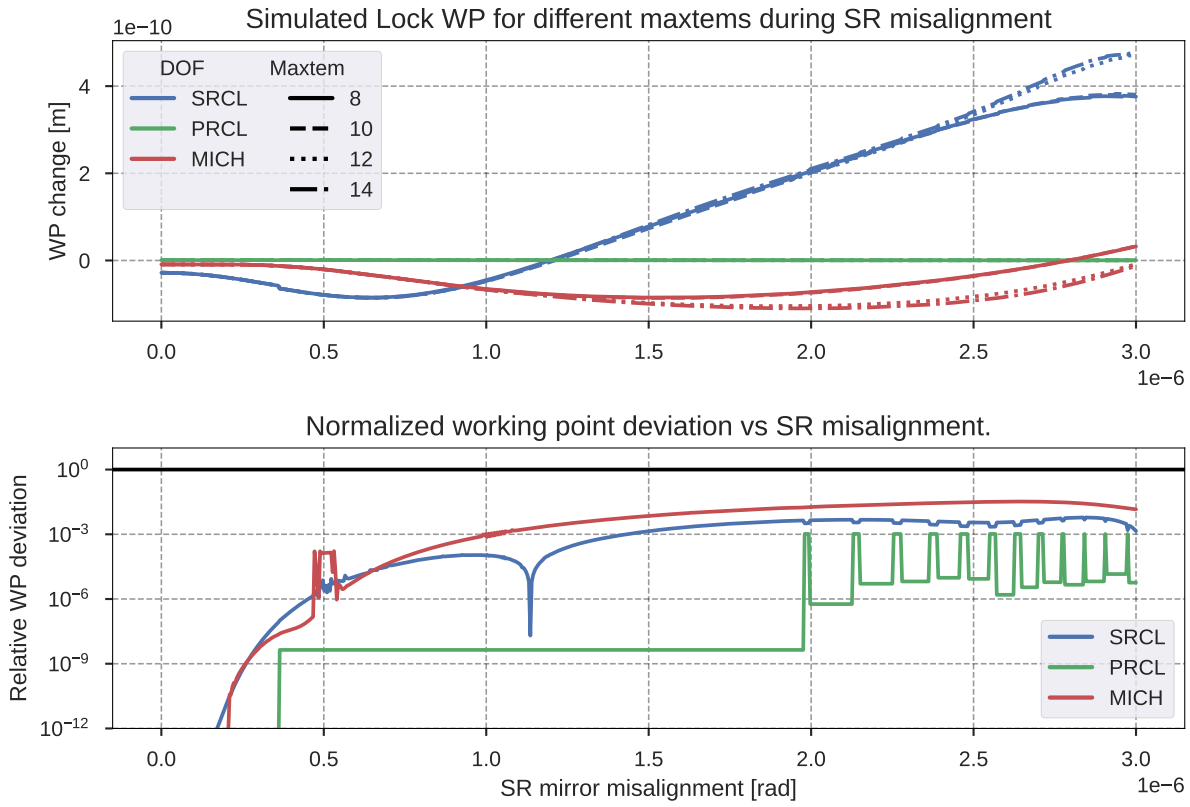

Figure 3: CITF DOFs' simulated WPs during the misalignment of the SR mirror for different 'maxtem' values. The DOFs are 'locked' using the '3f' signals. The 'maxtem' parameter indicates how many Hermite-Gauss HOMs were used in the simulation.
Bottom: Normalized WP differences for misalignments of the SR mirror. The lines indicate the difference in the WPs simulated with 'maxtem' 14 and 'maxtem' 12, normalized by the respective DOF accuracy requirements. Discontinuities in the line are caused by the finite tolerance of the lock algorithm.

as

$$\Theta := \arctan\left(\frac{\lambda}{\pi w_0}\right) \tag{1.1}$$

Where w_0 is the waist size of the beam. In the AdV+ interferometer, the waist size of the beam is $\simeq 10\ mm$, therefore giving an upper limit to the misalignment of $\Theta \simeq 35\ \mu rad$, well above the simulated angles.

1.3 Simulation of the longitudinal DOFs sweeps

. The initial simulations (described in section 1.2) allow to study the error signals at their working point and to estimate their optical gain, optimal demodulation phase, and cross-couplings. However, further simulations are required to check how the misalignment of the mirror affects the error signals in a region around the working points. These simulations use the required 'maxtem' values and WP found in the initial simulation. Therefore, we simulated longitudinal sweeps of one CITF LSC DOF at a time for a limited number of misalignment angles.

Simulating these sweeps allows checking the shape and linearity of the error signals around the working point, including checking for multiple zero-crossings. Additionally, the zero-crossing of the error signals can be compared with the resonance peaks of the carrier and (more importantly for this step of the lock acquisition) of the control sideband fields.

The longitudinal sweeps are simulated by displacing the mirrors corresponding to the studied DOF while keeping the others at the WP. During this step, the behaviour of the laser beam in the main interferometer ports is monitored in detail by virtual photodiodes and field amplitude detectors. Both I and Q quadrature of each error signal is acquired, allowing to emulate the demodulation at any wanted phase ϕ as follows:

$$Err[\phi] = \Re[(Err_I + iErr_Q)e^{-i\phi}] \tag{1.2}$$

1.4 Optimization and study of the error signals

This last step involves using the results of the simulations performed in the previous steps to study the behaviour of the error signals at different values of misalignment of the interferometer.

By setting the demodulation phase to the one used in the perfectly aligned condition, we studied the variation of multiple figures of merit against the misalignment of the CITF optics.

- Optical gains;
- working point;
- shape of the error signal (multiple zero crossings etc.).

As discussed in detail in the following section, the study of these quantities allows estimating a "threshold angle" beyond which the error signal cannot be used to keep the CITF locked.

Additionally, we studied how the optimal demodulation phases of each error signal changes with the misalignment, allowing us to estimate the increase of cross-couplings between the different DOFs.

2 Results

The planned error signals for the control of the CITF are listed in table 1, together with their respective optical gain in an optimally aligned configuration.

DOF	Errsig	Rel. OG [1/m]
PRCL	B2 18 (6.27*3) MHz	$2.6 \cdot 10^{-1}$
MICH	B2 169 (56.4*3) MHz Q	$8.2 \cdot 10^{-3}$
SRCL	B2 169 (56.4*3) MHz I	$5.7 \cdot 10^{-3}$

Table 1: CITF error "3f" error signals and relative optical gains. The optical gains of the error signal have been normalized by the power on the relative photodiode.

2.1 Optical Gain variation

One of the main effects of the misalignment is a progressive reduction of optical gain on the longitudinal Pound-Drever-Hall (PDH) error signals. The extent of this effect depends both on the error signal and on which mirror is misaligned. As expected, the simulations show that higher frequency PDH signals are overall less impacted by the misalignment than the lower frequency ones. This is due to the higher finesse of the later ones, less impacted by the Schnupp asymmetry losses towards the antisymmetric port.

The amount of gain loss that can affect a loop before it loses lock depends on several factors, in particular on the "gain margin" of the involved control loop and on the SNR of the error signal used. Automatic loop gain tuning processes based on a real-time estimate of the loop Unity Gain Frequency (UGF) help in maintaining the loop stable, as long as they "react" quickly enough. Even if compensated, a gain loss means a loss of Signal-to-Noise-Ratio (SNR) and an increase of re-injected sensing noise. Empirical experience tells us that an optical gain loss above a factor of 50% often leads to loss of control. For this reason, the misalignment angle at which this threshold is reached is an important figure of merit subject of this study. Figure 4, 5 and 6 show

the relative effect of PR, NI and SR mirror misalignments on the planned "3f" error signals' optical gains. The optical gains are normalized by the corresponding values in the aligned condition.

From the results, one can see that the most restrictive condition is given by the behaviour of the B2 18 MHz signal (used to control Power Recycling Cavity Length (PRCL)) for PR mirror misalignments. This error signal loses 50% of its optical gain at $5.7 \cdot 10^{-8}$ rad of PR misalignment (see figure 4).

This error signal is also the most affected by NI mirror misalignments, with a half-gain threshold of $7.8 \cdot 10^{-8}$ rad, as seen in figure 5.

SR misalignments instead have a much lower overall impact on the error signals (see figure 6, and, as expected, have more effect on the 56 MHz sidebands signals than on the 6 MHz ones due to the 56 MHz sidebands being resonant in the SR cavity. Additionally, the small MICHelson length (MICH) error signal gain increases with the SR mirror misalignment. No maximum threshold has been found for the simulated misalignments. Increasing the simulation range will eventually find a threshold given by the gain drop of Signal Recycling Cavity Length (SRCL) itself. However, this is not of interest for this study since the simulated misalignment is already well above the residual angular motion with the mirror under the control of the local controls alone ($\simeq 0.05 \mu rad$).

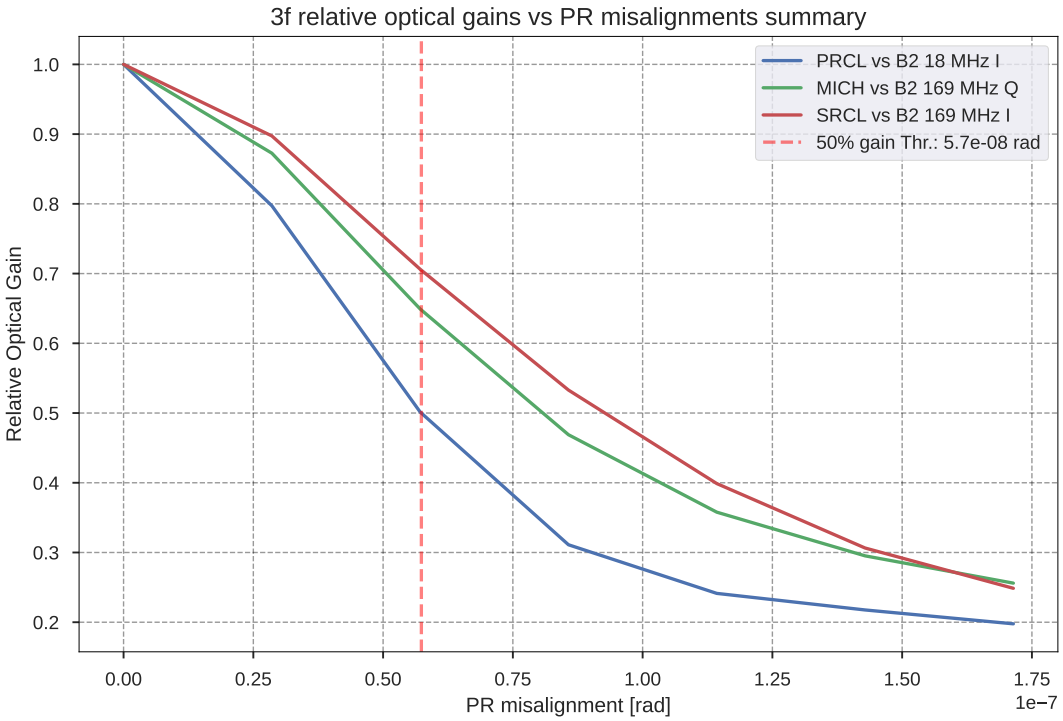

Figure 4: CITF error signals Optical Gain (OG) variation vs misalignments of the PR mirror. Each line corresponds to the relative optical gain of a "3f" error signal used for the control of the CITF. The OGs are relative to the gains in a fully aligned condition. The vertical line marks the lowest angle at which one of the error signals has lost 50% of its OG.

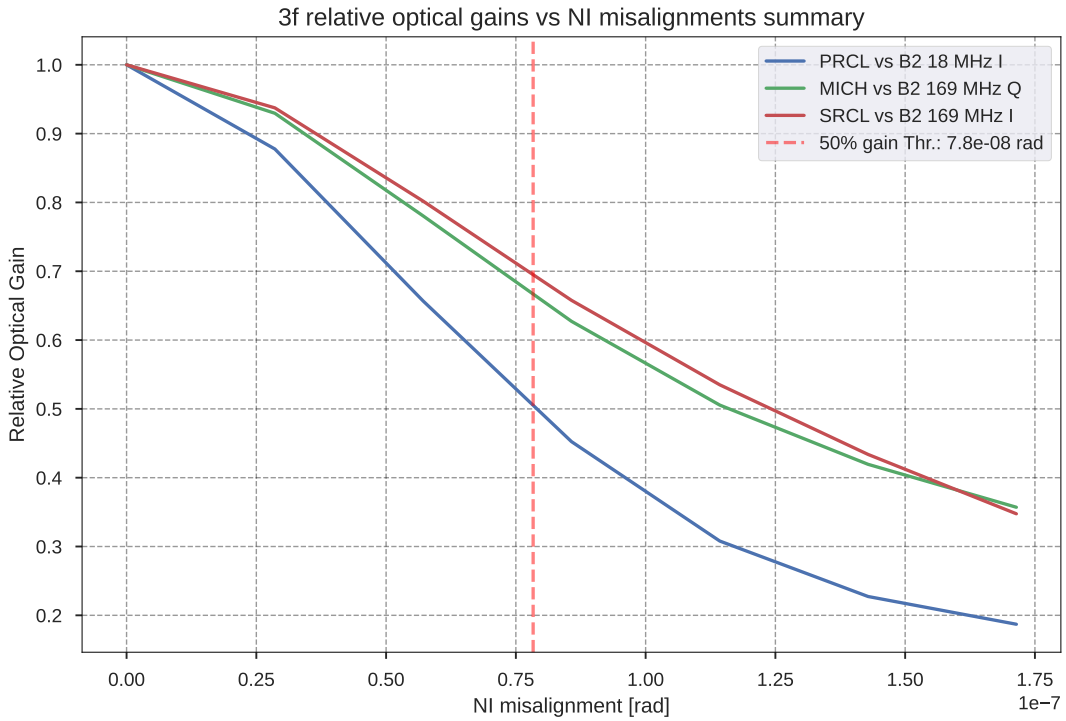

Figure 5: CITF error signals OG variation vs misalignments of the NI mirror. Each line corresponds to the relative optical gain of a "3f" error signal used for the control of the CITF. The OGs are relative to the gains in a fully aligned condition. The vertical line marks the lowest angle at which one of the error signals has lost 50% of its OG.

2.2 Error signal shapes and zero-crossing

The simulated DOF sweeps allowed to check for abnormalities in the error-signal shape and the correspondence of their zero-crossings with the control sideband peaks. The results for the "3f" error signals used to control the citf are represented in figures 7, 8 and 9, respectively, for the misalignment of the PR, NI and SR mirrors.

No particular concerns arise from the shapes of the error signals. At the simulated angles, the shape and the linear region of all the error signals are minimally affected, with the loss of optical gain as the noticeable main effect. The most noteworthy zero-crossing deviation is the SRCL error signal (B2 169MHz I), which, at the maximum simulated SR mirror misalignment, deviates $\simeq 1.7\ nm$ from the 56 MHz sideband peak observed by the B2 112 MHz magnitude signal. However, as mentioned above, the maximum simulated SR misalignment ($\simeq 3\ \mu rad$) represents an unlikely scenario, even with the alignment controlled by local controls. Lower SR misalignments or large PR and NI misalignments also introduce a similar deviation but of negligible magnitude ($\leq 0.5\ nm$).

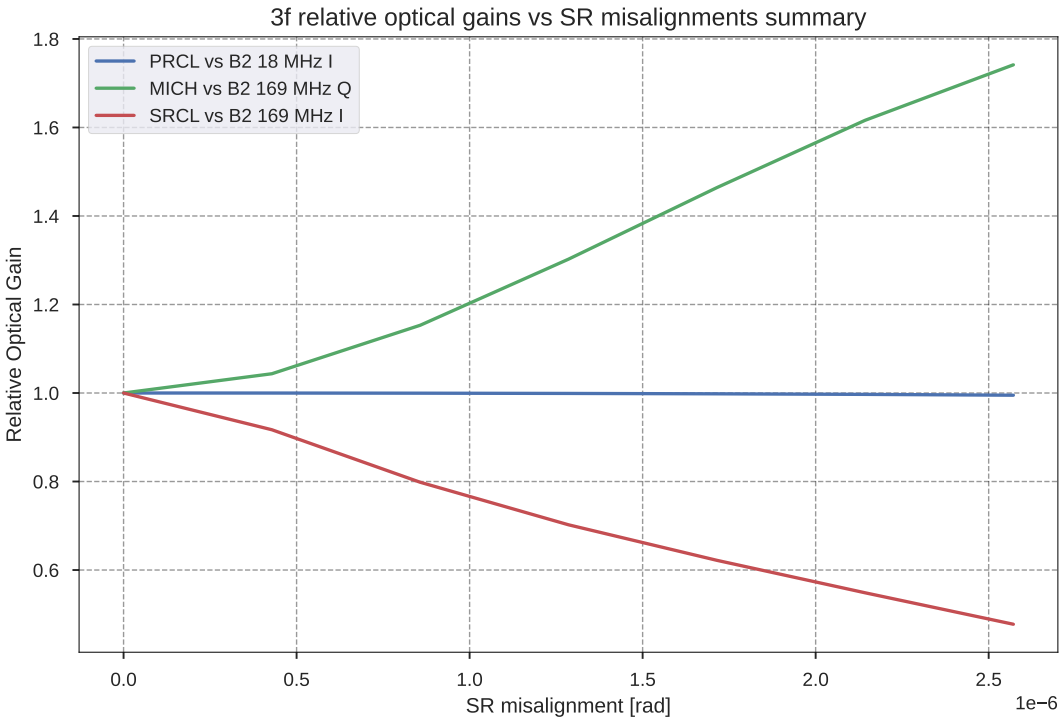

Figure 6: CITF error signals OG variation vs misalignments of the SR mirror. Each line corresponds to the relative optical gain of a "3f" error signal used for the control of the CITF. The OGs are relative to the gains in a fully aligned condition. The vertical line marks the lowest angle at which one of the error signals has lost 50% of its OG.

2.3 Optimal demodulation phase variations

Each error signal is demodulated at the phase that maximizes the optical gain against the displacement of the respective DOF. A mirror misalignment can change the optimal demodulation phases and, consequently, introduce cross-couplings between different DOFs and reduce the overall SNR. A variation of optimal demodulation phase larger than 90° means a change of sign of the error signal, but usually, the lock fails much before reaching this point. Changes larger than $20 - 30°$ usually are enough to cause an unlock.

Figure 10, 11, and 12 show the change in the demodulation phase of the main error signals for misalignments of the PR, NI and SR mirrors, respectively. From the results, one can see that the change in the optimal demodulation phase is always lower than 10° for misalignments lower than the thresholds found looking at the optical gain variations in section 2.1. Therefore, the change in the demodulation phase is not the limiting factor in the allowed misalignment.

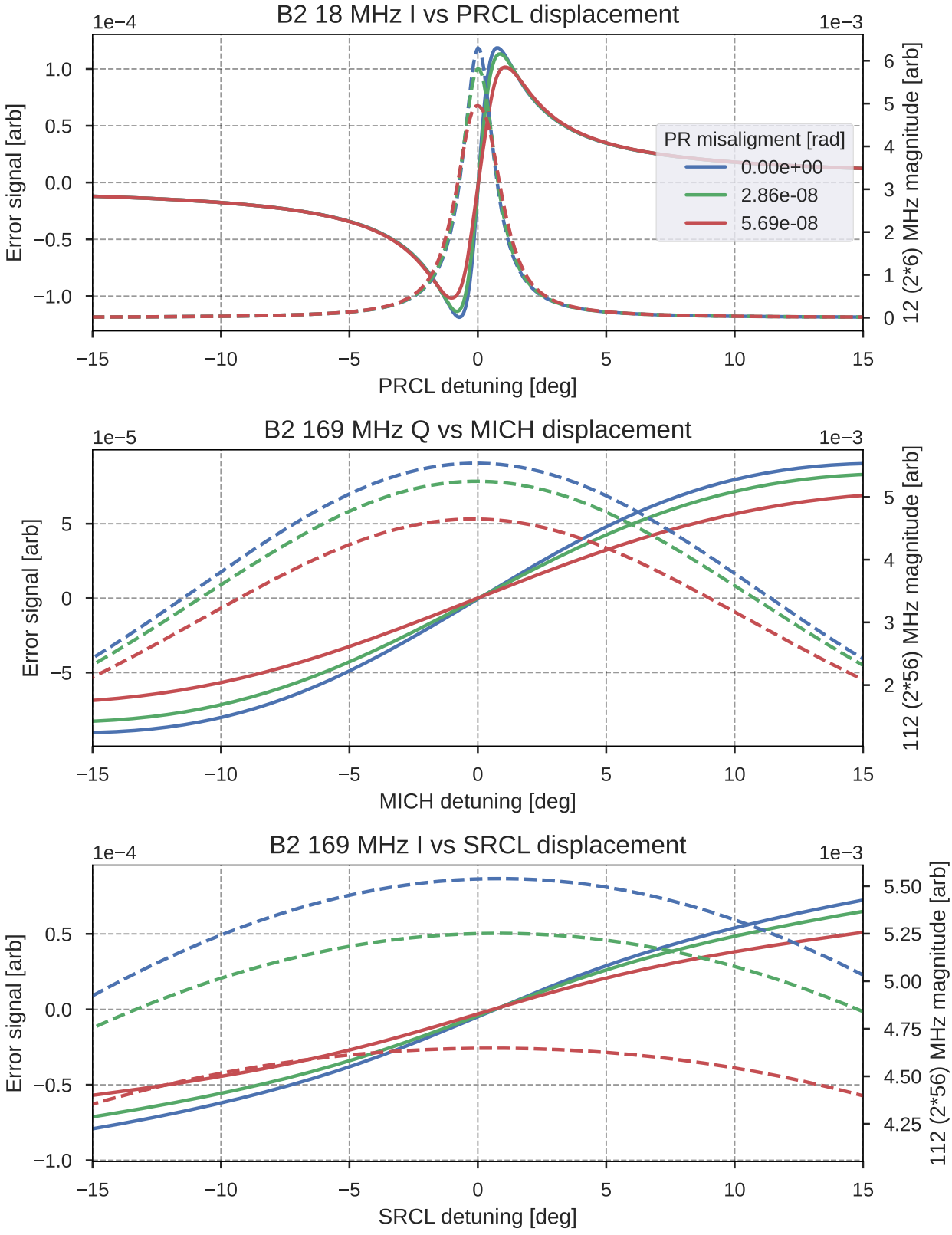

Figure 7: CITF error signals scans for various PR misalignments. Each plot shows the scan of a different CITF dof and its corresponding "3f" error signal (continuous lines). The dashed lines show the "2f" signal magnitude corresponding to either the 6 MHz (first plot) or 56 MHz (second and third plot) resonances.

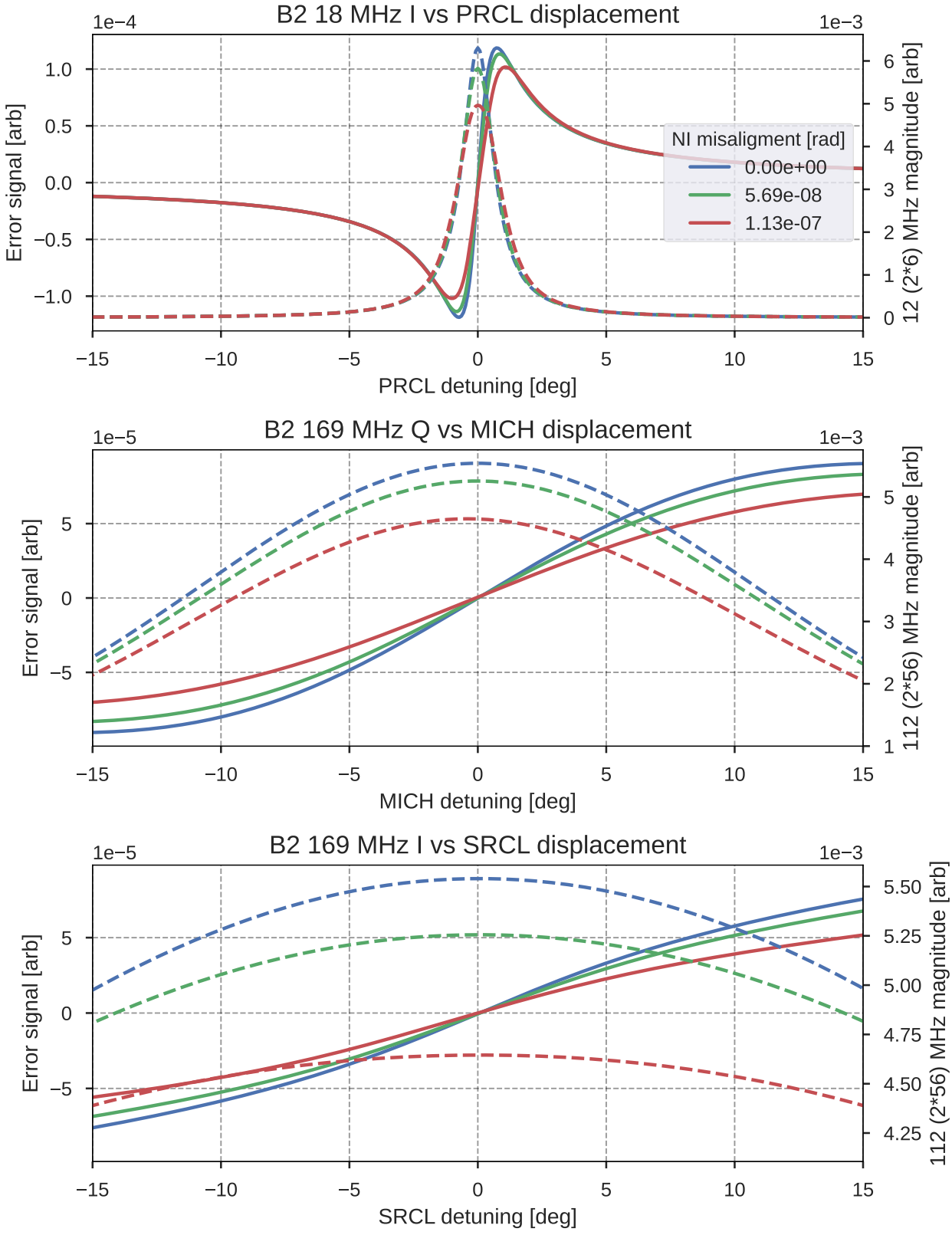

Figure 8: CITF error signals scans for various NI misalignments. Each plot shows the scan of a different CITF dof and its corresponding "3f" error signal (continuous lines). The dashed lines show the "2f" signal magnitude corresponding to either the 6 MHz (first plot) or 56 MHz (second and third plot) resonances.

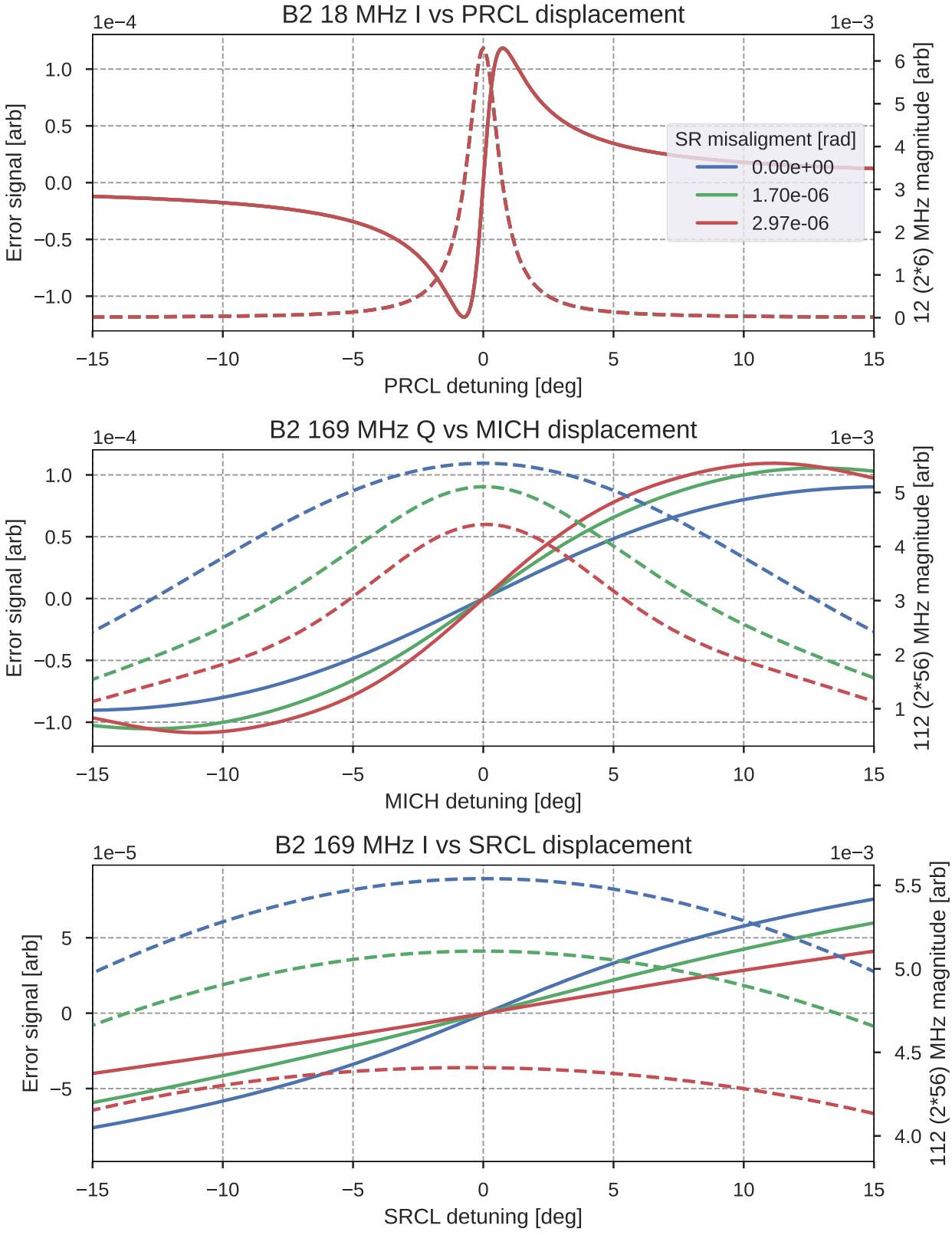

Figure 9: CITF error signals scans for various SR misalignments. Each plot shows the scan of a different CITF dof and its corresponding "3f" error signal (continuous lines). The dashed lines show the "2f" signal magnitude corresponding to either the 6 MHz (first plot) or 56 MHz (second and third plot) resonances.

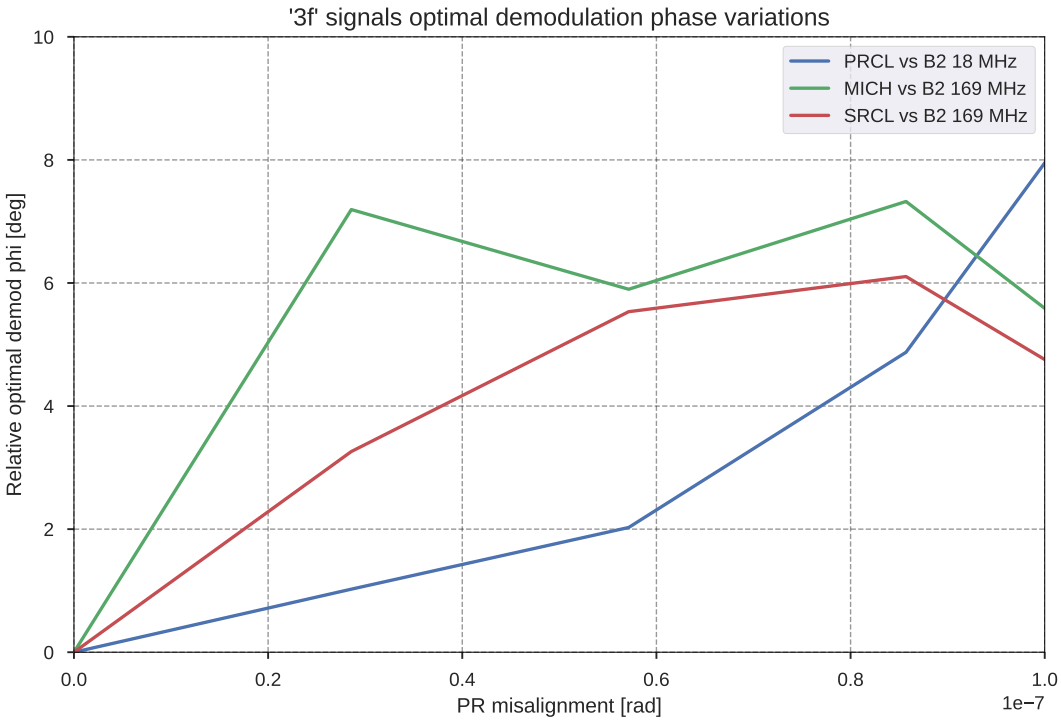

Figure 10: Variation of the optimal demodulation phase for the main "3f" error signals against misalignments of the PR mirror.

2.4 Cross couplings

Another effect that has been studied is the influence of the misalignment in the couplings between different DOFs.

Figure 13, 14, and 15 compare, at each studied misalignment, the optical gain of each error signal against the three different CITF DOFs. The optical gains of each signal (each column) have been divided by the optical gains of the corresponding controlled DOF[1].

Results: The results show that PRCL has a large impact on all the error signals, and its error signal (B2 18 MHz) is minimally influenced by MICH and SRCL displacements, even at high misalignments. Nevertheless, due to its high optical gain (see table 1), the PRCL loop can be closed with a much higher gain and bandwidth than the MICH and SRCL ones. This allows suppressing PRCL residual motion at the level of having little impact on MICH and SRCL.

Indeed, experimental results confirmed that the PRCL loop is stable up to an UGF of $\simeq 70Hz$, while SRCL and MICH are respectively kept at UGF of $\simeq 5Hz$ and $\simeq 15Hz$ during the lock acquisition. Additionally, the phase of the MICH error signal (B2 169 MHz Q) is maintained as orthogonal as possible to the optimal PRCL phase, minimizing the influence of its displacement. This has the downside of maximizing the impact of PRCL displacements on the SRCL loop, but since this loop has the lowest bandwidth and the largest linear region, its robustness is not affected by this cross-coupling.

SRCL detuning has a low impact on all error signals for any misalignment angle, not raising particular concerns.

The MICH displacement impact on the PRCL error signal remains negligible. Its impact on the SRCL error

[1] e.g., plots in the first column (corresponding to the B2 18 MHz I signal) have been divided by the OG of B2 18 MHz I for PRCL

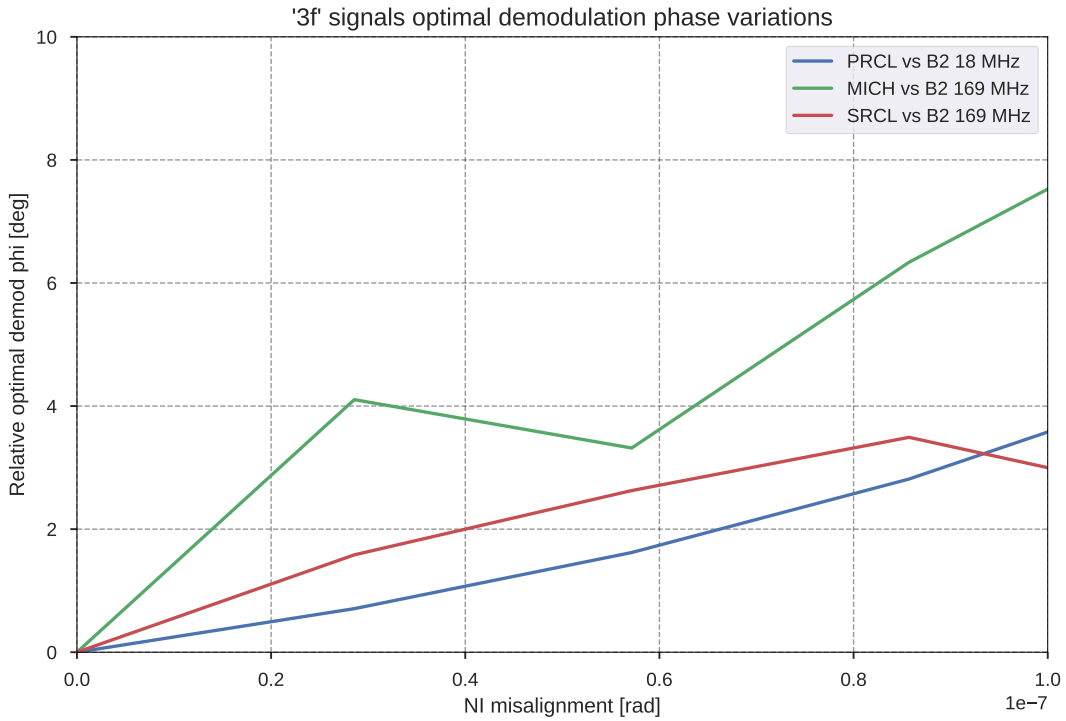

Figure 11: Variation of the optimal demodulation phase for the main "3f" error signals against misalignments of the NI mirror.

signal (B2 169 MHz I) instead increases by a factor of $\simeq 2$ for PR and NI misalignments above $0.5 \cdot 10^{-}7$ rad (figure 13 and 14, respectively). Considering that the MICH impact remains a factor 4 below the SRCL gain and considering the high robustness and low UGF of the SRCL loop, the main limiting factor to the NI and PR misalignment remains the loss of optical gains discussed in section 2.1.

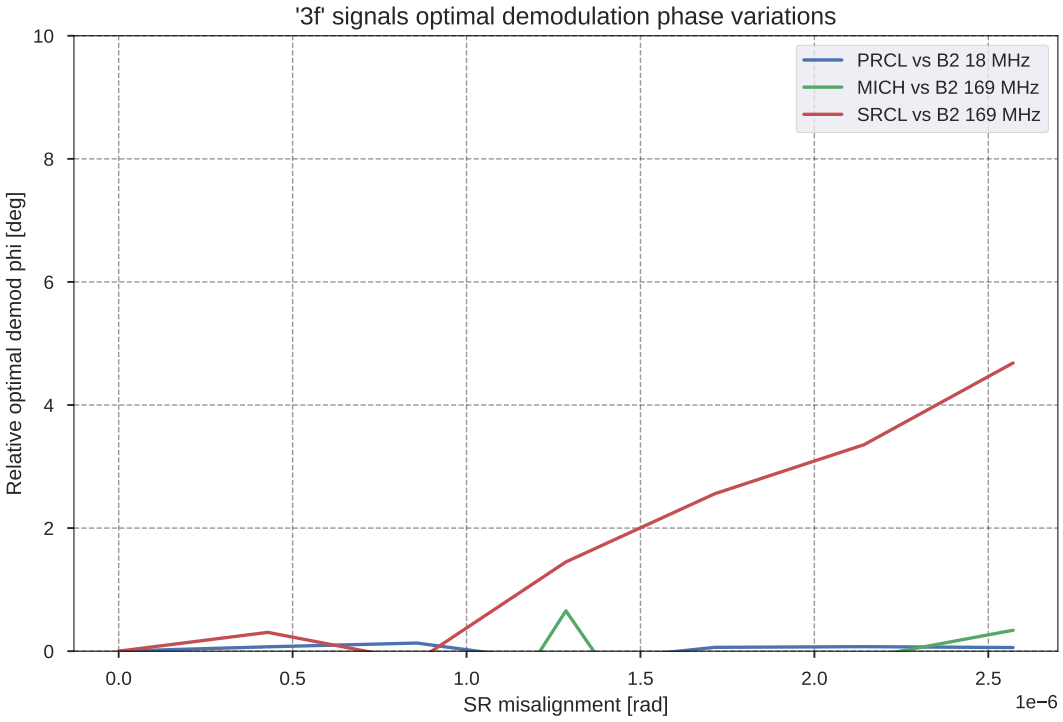

Figure 12: Variation of the optimal demodulation phase for the main "3f" error signals against misalignments of the SR mirror.

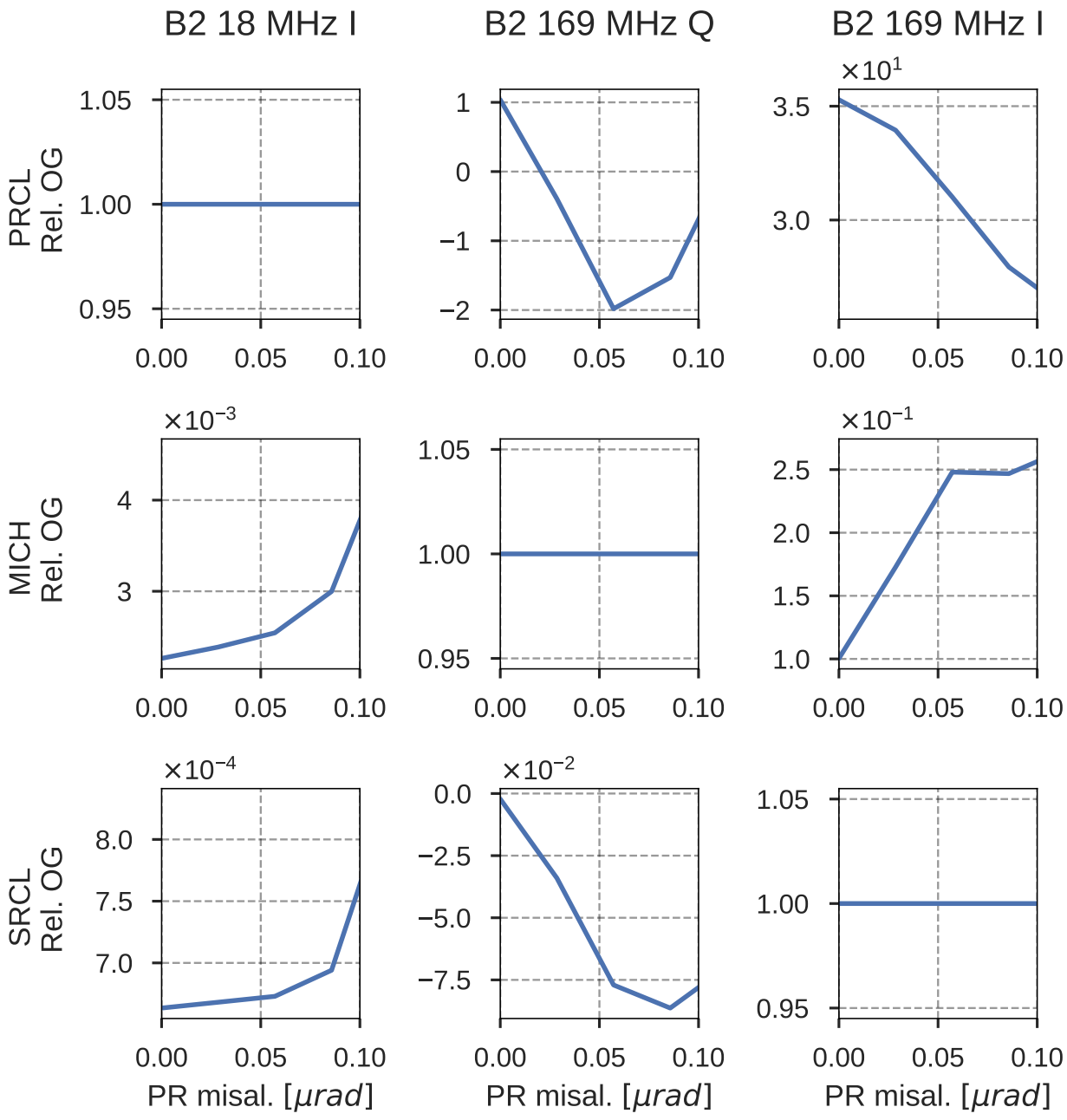

Figure 13: Evolution of cross-couplings between CITF DOFs for misalignments of the PR mirror. Each column corresponds to a different error signal, each row to a different DOF. Each plot shows the relative OG of the respective error signal against displacements of the respective DOF. The OGs are divided by the OG of the diagonal elements, corresponding to the OG of the signals used in the feedback loops.

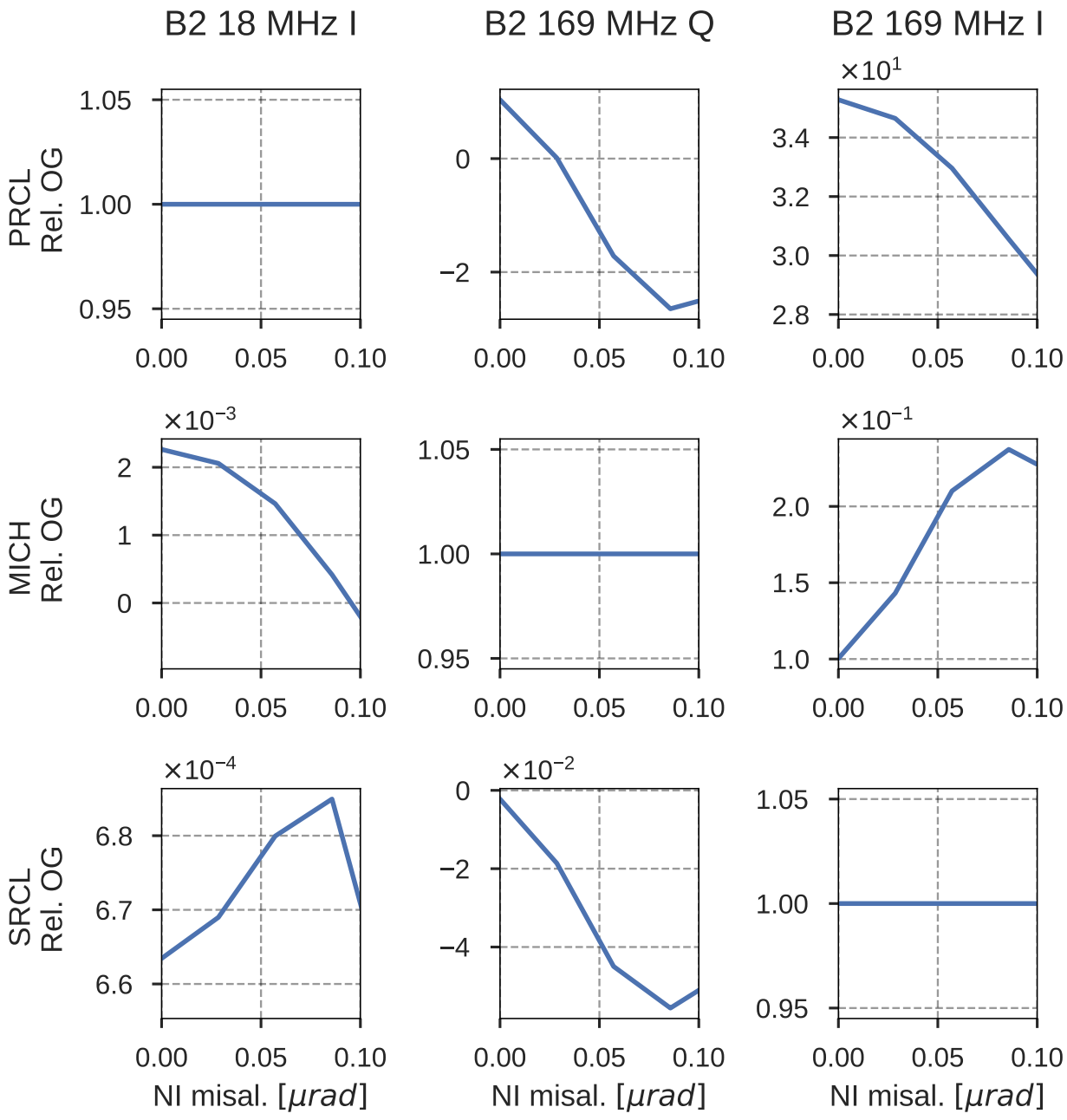

Figure 14: Evolution of cross-couplings between CITF DOFs for misalignments of the NI mirror. Each column corresponds to a different error signal, each row to a different DOF. Each plot shows the relative OG of the respective error signal against displacements of the respective DOF. The OGs are divided by the OG of the diagonal elements, corresponding to the OG of the signals used in the feedback loops.

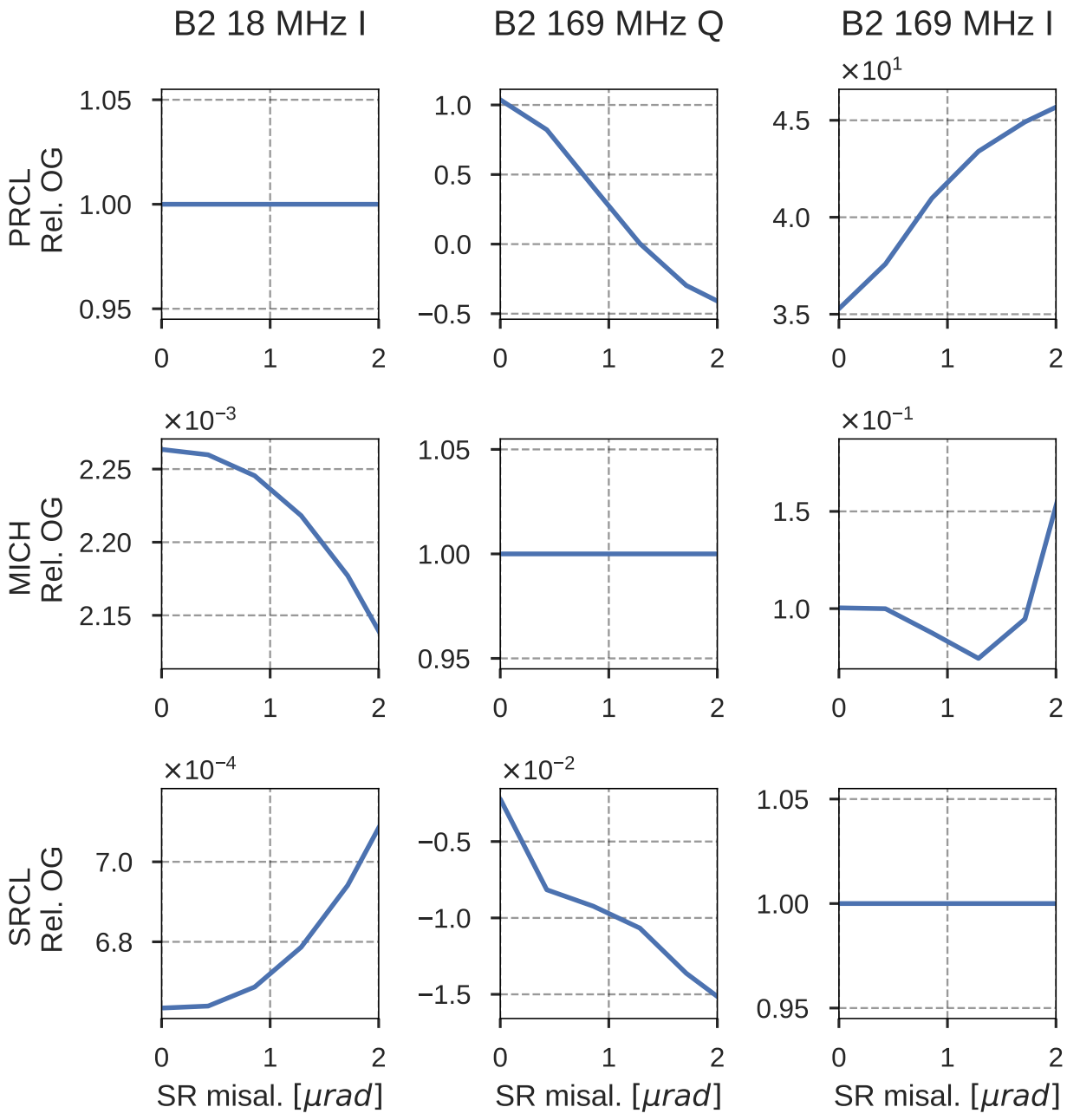

Figure 15: Evolution of cross-couplings between CITF DOFs for misalignments of the SR mirror. Each column corresponds to a different error signal, each row to a different DOF. Each plot shows the relative OG of the respective error signal against displacements of the respective DOF. The OGs are divided by the OG of the diagonal elements, corresponding to the OG of the signals used in the feedback loops.

3 Conclusions

The most restrictive result of the simulation is given by the impact of PR misalignment on the error signals' optical gains. Its "half-gain-loss" threshold of $5.7 \cdot 10^{-8}$ *rad* is very close to the residual angular noise of optimized local controls.

A slightly less strict threshold ($7.8 \cdot 10^{-8}$ *rad*) has been found for the NI misalignment, given by the "half-gain-loss" in this case too.

The other studied figures of merit (optimal demodulation phase changes, different DOFs cross-couplings, changes in error signal shape and linearity) did not show effects of comparable impact on the lock at the studied misalignment angles.

Following the preliminary results of this study, automatic-alignment error signals were carried out [7], with the aim of finding possible error signals for the control of the angular degrees of freedom in the DRMI configuration, with particular focus to the PR mirror alignment.

Commissioning results [8] confirmed the large effect of the PR alignment on the stability of the DRMI lock. This effect was particularly detrimental also due to specific limitations ([9]) in the accuracy of the PR mirror optical levers, which result in worse accuracy of its local controls with respect to other mirrors. The engagement the its full-bandwidth automatic alignment control loop as soon as the longitudinal lock is achieved is necessary to maintain it for longer than a few seconds.

Acronyms

ALS Auxiliary Laser System. 2

ASC Angular Sensing and Control. 2

CARM Common ARM length. 2

CITF Central InTerFerometer. 2–13, 18–20

DARM Differential ARM length. 2

DOF Degree Of Freedom. 2–6, 8, 9, 13, 18–20

DRMI Dual-Recycled Michelson Interferometer. 2

HOM Higher Order Mode. 2–5

IR InfraRed. 2

LSC Longitudinal Sensing and Control. 3, 5

MICH small MICHelson length. 7, 13, 14

NI North Input. 3, 4, 7–9, 11, 14, 19

OG Optical Gain. 7–9, 13, 18–20

PDH Pound-Drever-Hall. 6

PR Power Recycling. 2–4, 7–10, 13, 14, 18

PRC Power Recycling Cavity. 7

PRCL Power Recycling Cavity Length. 13

PRMI Power-Recycled Michelson Interferometer. 2

SNR Signal-to-Noise-Ratio. 6, 9

SR Signal Recycling. 2–5, 7–9, 12, 15, 20

SRCL Signal Recycling Cavity Length. 7, 8, 13, 14

TEM Transverse ElectroMagnetic. 3

UGF Unity Gain Frequency. 6, 13, 14

WP Working Point. 3–6

References

[1] Annalisa Allocca, Antonino Chiummo, and Maddalena Mantovani. *Locking Strategy for the Advanced Virgo Central Interferometer*. 2016. URL: https://tds.virgo-gw.eu/ql/?c=11495.

[2] Julia Casanueva Diaz and N. Leroy. *Auxiliary Laser System: Study of the Lock Acquisition Strategy*. Apr. 1, 2019. URL: https://tds.virgo-gw.eu/ql/?c=14154.

[3] Daniel David Brown and Andreas Freise. *Finesse*. May 19, 2014. DOI: 10.5281/zenodo.821364. URL: https://zenodo.org/record/821364.

[4] Michele Valentini et al. *Error Signals for the Longitudinal Controls in Dual Recycled Advanced Virgo Interferometer - Steady State*. May 11, 2020. URL: https://tds.virgo-gw.eu/ql/?c=15570.

[5] Priyanka Giri et al. "Effects of Cold Aberrations on the Longitudinal Error Signals and Its Compensation". In: *Proceedings of The European Physical Society Conference on High Energy Physics â PoS(EPS-HEP2021)*. The European Physical Society Conference on High Energy Physics. Vol. 398. SISSA Medialab, May 12, 2022, p. 069. DOI: 10.22323/1.398.0069. URL: https://pos.sissa.it/398/069.

[6] Michele Valentini et al. *Update of the LSC Accuracy Requirements for AdV +*. Technical report. Mar. 29, 2021. URL: https://tds.virgo-gw.eu/ql/?c=15030.

[7] Mattia Boldrini et al. *Simulation of the Angular Sensing for the Central Interferometer in Advanced Virgo+*. Oct. 3, 2021. URL: https://tds.virgo-gw.eu/ql/?c=16597.

[8] Julia Casanueva Diaz and Mattia Boldrini. *ISC Shift: CITF Lock Robustness*. Logbook Entry. Mar. 26, 2021. URL: https://logbook.virgo-gw.eu/virgo/?r=51228.

[9] Ettore Majorana. *PR TY Investigations*. Oct. 21, 2. URL: https://logbook.virgo-gw.eu/virgo/?r=53350.